

## IDENTIFICATION AND SELECTION OF ROTORCRAFT CANDIDATE MODELS TO PREDICT HANDLING QUALITIES AND DYNAMIC STABILITY

Johannes Wartmann, DLR (German Aerospace Center), Braunschweig, Germany  
Steffen Greiser, DLR (German Aerospace Center), Braunschweig, Germany

### Abstract

Current frequency-domain system identification methods require an open-loop experiment design for data collection to identify one model of a vehicle. This makes open-loop system identification for unstable systems like rotorcrafts challenging. The optimized Predictor-Based Subspace Identification method also estimates accurate models from closed-loop data. In this paper, a parameter study is conducted to identify a set of bare airframe models of the ACT/FHS research rotorcraft using this subspace method. A selection method is introduced to choose appropriate candidate models from the identified set. The selected candidate models differ slightly in terms of the model invariants and are all a valid approximation of the rotorcraft dynamics. Consequently, the selected candidate models can be used to predict the possible properties of the system and their uncertainties. Here, the candidate models are employed to estimate the dynamic stability and handling qualities of the ACT/FHS bare airframe and two control systems of the ACT/FHS research rotorcraft.

### NOTATION

ACT/FHS	Active Control Technology / Flying Helicopter Simulator
ARX	AutoRegressive model with eXogenous input
DLR	Deutsches Zentrum für Luft- und Raumfahrt (German Aerospace Center)
FR	(measured) frequency response
HQ	handling qualities
PBSIDopt	optimized Predictor-Based Subspace Identification (method)
rms	root mean square (error)
SCAS	stability control augmentation system
$A, B, C, D$	discrete-time state-space matrices
$A_{ct}, B_{ct}, C_{ct}$	continuous-time state-space matrices
$A_K, B_K$	predictor form state-space matrices
$d_1, \underline{d}_1$	index of agreement, overall $d_1$

$D$	damping coefficient
$e_k, u_k, x_k, y_k$	discrete-time innovation, input, state and output vectors at $k$ -th time step
$E, U, X, Y$	data matrices for system innovations, inputs, states and outputs (used with indexes)
$f, p$	future, past window length
$K$	feedback controller gain
$K$	Kalman gain matrix
$M_n, M_p$	sets for $n$ and $p$
$n$	number of states (model order)
$n_u, n_y$	number of inputs, number of outputs
$N$	number of measurements
$p, q, r$	roll, pitch and yaw rates, rad/s
$T_P$	time period, s
$u, v, w$	aircraft fixed airspeed components, m/s
$x_0, y_0$	initial state, output offset
$y_{m,k}$	measured output (index $m$ )
$z_k$	$k$ -th merged input-output vector
$Z$	data matrices for merged input-outputs (used with indexes)
$\mathcal{K}^{(p)}$	extended controllability matrix
$\mathcal{O}^{(f)}$	extended observability matrix
$S$	diagonal singular value matrix
$\delta_x, \delta_y$	longitudinal and lateral cyclic controls, %
$\delta_p, \delta_0$	pedal and collective controls, %
$\lambda$	regularization parameter
$\sigma(\cdot)$	standard deviation
$\phi, \theta$	roll and pitch attitude angles, rad

### Copyright Statement

The authors confirm that they, and/or their company or organization, hold copyright on all of the original material included in this paper. The authors also confirm that they have obtained permission, from the copyright holder of any third party material included in this paper, to publish it as part of their paper. The authors confirm that they give permission, or have obtained permission from the copyright holder of this paper, for the publication and distribution of this paper as part of the ERF proceedings or as individual offprints from the proceedings and for inclusion in a freely accessible web-based repository.

## 1. INTRODUCTION

Common rotorcraft system identification approaches use frequency-domain methods to identify linear models of the corresponding vehicle. Depending on the complexity of the model and whether rotor or engine states are included, the identified models can be accurate for frequencies up to 30 rad/s as described in ref.<sup>1</sup>. The identification of such complex models using frequency-domain methods and the appropriate generation of the flight test data is a laborious task, but essential to gain useful rotorcraft models for analysis, simulation, and flight control.

During the last decade, physics-based models of DLR's research helicopter EC135 ACT/FHS (Active Control Technology/Flying Helicopter Simulator) have been identified using a Maximum Likelihood frequency-domain method, see refs.<sup>2-6</sup> amongst others. For this task, dedicated flight tests have been conducted for system identification and model validation with the ACT/FHS research rotorcraft. The system identification flight tests consist of at least two manual frequency sweeps with increasing frequency for each control input and reference airspeed. This approach is considered to give good identification results of the bare airframe dynamics in an open-loop experiment design using the approved system identification methods in the frequency domain.

Today, state of the art system identification methods like the optimized Predictor-based Subspace Identification method (PBSIDopt) offer the possibility to estimate models for systems with multiple inputs and outputs without the definition of a model structure beforehand. The PBSIDopt method directly operates on the measured input-output data in the time domain and is able to estimate asymptotically unbiased models from noisy closed-loop data, see refs.<sup>7-9</sup>. The ACT/FHS research rotorcraft was identified using the PBSIDopt method in ref.<sup>10</sup> and ref.<sup>11</sup> using the open-loop flight test data. The resulting high-order models provided good to excellent accuracy (regarding the rms errors) and the resulting model states were interpreted physically using the system's eigenvalues and eigenvectors. Furthermore, multiple-input closed-loop system identification maneuvers were developed and evaluated to identify the bare airframe dynamics of the ACT/FHS rotorcraft simulator to simplify the laborious flight tests for system identification. This was the first step at the DLR to prepare the PBSIDopt method for the application in rotorcraft series production, see ref.<sup>12</sup>.

This paper presents a novel approach to gain reliable candidate models from flight test data to pre-

dict possible properties of the system to be identified. This approach is the second step to use system identification in rotorcraft series production applying the PBSIDopt method. For that purpose, a parameter variation study is conducted identifying a set of linear state-space models of the ACT/FHS research rotorcraft applying the PBSIDopt method to dedicated flight test data. The contribution of this paper is new a method to select a subset of reliable candidate models from the identified model set. The chosen candidate models represent the dynamics of the rotorcraft appropriately and differ slightly in terms of the model invariants, i.e. eigenvalues, zeros and input-output transfer functions. In general, only one model is used to determine the system's properties and no uncertainties are accounted for. In this paper, the chosen candidate models are used to predict the possible vehicle characteristics and their uncertainties, since flight tests does not show a unique property of the system, but a range of possible properties, e.g. for a system's response. In detail, the dynamic stability and the handling qualities (HQ) of the ACT/FHS bare airframe are evaluated using the candidate models. In addition, the possible HQ of two control systems for the ACT/FHS are investigated. The paper finishes with conclusions and an outlook for future work.

## 2. EXPERIMENTAL SETUP

### 2.1. The ACT/FHS Research Rotorcraft

The ACT/FHS, shown in figure 1, is the main test-bed for rotorcraft research at DLR, see ref.<sup>13</sup>. This rotorcraft is a twin-engine helicopter with fenestron and bearingless main rotor and a maximum take-off weight of about 2.9 t based on a highly modified Airbus Helicopters EC135 (former Eurocopter).



Figure 1: DLR's research rotorcraft ACT/FHS

The ACT/FHS has a full-authority fly-by-wire/fly-by-light control system which complement its mechanical controls to allow actuator inputs generated by an experimental system in flight. Therefore, the dynamics of the ACT/FHS are not comparable to

data from a production EC135 (or H135) rotorcraft. The ACT/FHS is fitted with various sensors (e.g. a noseboom, two differential GPS receivers, flight test instrumentation and a high-quality inertial measurement system). Experimental system identification of the ACT/FHS yields the necessary models for the model-based control and in-flight simulation research activities at DLR.

## 2.2. Flight Test Data

Dedicated flight tests with the ACT/FHS research rotorcraft for system identification and model validation were conducted in 2009 and 2010. These flight tests consist of at least two manual frequency sweeps with increasing frequency up to about 2 Hz for each control input at each of the five reference airspeeds (i.e. hover, 30, 60, 90, and 120 knots). During the manual frequency sweeps, a flight state near the reference trim condition has been maintained by applying uncorrelated, pulse-type inputs on the secondary controls only. In this way, cross-correlations between the four control inputs are minimized. At the same flight conditions, computer-generated 3211-multistep input maneuvers have been recorded as a dissimilar basis for model validation purposes.

For this paper, eight manual frequency sweeps at 60 knots have been selected from the system identification database. Furthermore, eight 3211-multistep maneuvers at the same airspeed have been chosen for model validation. The selected maneuvers, the applied control amplitudes and the test durations are summarized in table 1.

Table 1: ACT/FHS system identification and model validation maneuvers at 60 knots forward flight

maneuver	control axis amplitude	
2x manual sweep	$\delta_x$	max. 10 %
2x manual sweep	$\delta_y$	max. 10 %
2x manual sweep	$\delta_p$	max. 15 %
2x manual sweep	$\delta_0$	max. 11 %
2x automatic 3211	$\delta_x$	$\pm 4$ %
2x automatic 3211	$\delta_y$	$\pm 4$ %
2x automatic 3211	$\delta_p$	$\pm 9$ %
2x automatic 3211	$\delta_0$	$\pm 6$ %

## 2.3. Flight Path Reconstruction and Data Pre-Processing

A flight path reconstruction is used to estimate the motion of the rotorcraft's center of gravity and the local wind from raw sensor data after flight, since

the corresponding rotorcraft states are not measured directly. The flight path reconstruction is a post-flight process using two Unscented Kalman Filters consecutively to estimate the rotatory and translatory states of the rotorcraft. Both Unscented Kalman Filters and the used sensors are described in detail in ref.<sup>14</sup>.

In addition, the estimated states are processed by two separate Unscented Rauch-Tung-Striebel Smoothers described in ref.<sup>15</sup>. Thus, the estimated states are smoothed in an optimal sense without an additional phase delay. Measured signals that are not included in the flight path reconstruction, i.e. the helicopter controls are provided with the a synchronized sampling time of the experimental system. Since the maximum frequency of interest is about 35 rad/s all data is down-sampled to 40 ms which provides a Nyquist frequency twice as high. The reduced sampling time is beneficial to lower the computational costs for system identification.

## 3. SYSTEM IDENTIFICATION

The applied PBSIDopt method yields a linear continuous-time state-space model of the form

$$(1a) \quad \dot{x} = A_{ct}x + B_{ct}u$$

$$(1b) \quad y = C_{ct}x.$$

and required a finite number  $k = 1 \dots N$  of data points for the inputs  $u_k$  and outputs  $y_k$  respectively. This subspace method transforms the system identification problem into a high-order vector-ARX model (AutoRegressive model with eXogenous inputs). This is solved by a regularized least-squares approach. Then, the models states are reconstructed applying a singular value decomposition on ARX parameters. Subsequently, the discrete-time system matrices are estimated using the known inputs and outputs, as well as the calculated model states. The discrete-time model is transformed into continuous-time representation via a zero-order hold.

More details about the applied PBSIDopt method can be found in the appendix at the end of the paper.

### 3.1. Identification of ACT/FHS models

The four helicopter controls for longitudinal and lateral cyclic, pedal, and collective are used as system identification inputs,  $u_k$ . The body fixed airspeed components  $u, v, w$ , the angular rates  $p, q, r$  as well as the roll and pitch attitude angles  $\phi$  and  $\theta$  of the

aircraft are used as outputs  $y_k$ :

$$(2a) \quad \mathbf{u}_k = (\delta_x \quad \delta_y \quad \delta_p \quad \delta_0)^T,$$

$$(2b) \quad \mathbf{y}_k = (u \quad v \quad w \quad p \quad q \quad r \quad \phi \quad \theta)^T.$$

In addition to the model order  $n$ , the past window length  $p$  and the future window length  $f$  have a major influence on the accuracy of the identified models and their invariant characteristics like the system eigenvalues. Several guidelines exist to define these parameters, see<sup>7-9</sup>. Nonetheless, determining an optimal  $p$  and  $f$  is still active research and is still very time consuming. For this reason, a parameter variation study with respect to  $p$ ,  $f$  and  $n$  is conducted to identify many linear state-space models of the ACT/FHS research rotorcraft, see also<sup>10-12</sup>. Parameter studies are fast on modern desktop computers. Hence, a huge range of suitable parameter settings are tested in this paper. The values for the past window length  $p$  and the future window length  $f$  are

$$(3a) \quad p \in M_p | M_p = \{20 \ 30 \ 40 \dots 990 \ p_{\max}\},$$

$$(3b) \quad f \in M_f : f \leq p.$$

The past window length is limited to  $p_{\max} = 994$  to avoid the underdetermined case of the least-squares problem in equation (A.9). The maximum past window length is given by

$$(4) \quad p_{\max} = \frac{\sum N_j}{n_u + n_y + \sum j}$$

with the number of samples  $N_j$  of each maneuver  $j$ .

In this paper, models with an order between  $n = 8$  and  $n = 20$  are identified:

$$(5) \quad n \in M_n | M_n = \{8 \ 9 \dots 20\}.$$

In summary, 4,950 models of the ACT/FHS are identified (and validated) for each chosen model order  $n$ . The overall identification and validation process took about 65 h on a standard desktop computer.

### 3.2. Model Validation

All identified models are validated in the time domain to gain a comparable model performance measure. For each control axis an automatic 3211-multistep maneuver with positive and negative control deflection starting in the trim point is used for model validation. In total, eight 3211-multistep maneuvers are available for model validation. The model validation procedure consists of the estimation

of the initial model states  $x_0$  and output offsets  $y_0$  for every linear continuous-time state-space model and each maneuver, respectively.

The overall simulated model output  $y(t)$  is the superposition of the output for  $x_0 = \mathbf{0}$ , the output offsets  $y_0$  and the reaction of  $x_0$  on the model output:

$$(6) \quad y(t) = y(t, x_0 = \mathbf{0}, y_0 = \mathbf{0}) + y_0 + C_{ct} e^{A_{ct} t} x_0$$

with the matrix exponential of the state matrix multiplied by time  $e^{A_{ct} t}$ .

Thus, the initial model states  $x_0$  and output offsets  $y_0$  can be effectively estimated solving a least-squares problem which minimizes the difference between the output error  $y_e$  and the last two terms in equation (6). The output error  $y_e$  between the simulated model output with  $x_0 = \mathbf{0}$  and the measurements is

$$(7) \quad y_e = y_m - y(x_0 = \mathbf{0}, y_0 = \mathbf{0}).$$

An effective way to solve this optimization problem is to set up a system of linear equations

$$(8) \quad \begin{pmatrix} y_e(t = t_0) \\ y_e(t = t_1) \\ \vdots \\ y_e(t = t_e) \end{pmatrix} = \underbrace{\begin{pmatrix} C_{ct} e^{A_{ct} t_0} & I \\ C_{ct} e^{A_{ct} t_1} & I \\ \vdots & \vdots \\ C_{ct} e^{A_{ct} t_e} & I \end{pmatrix}}_H \begin{pmatrix} x_0 \\ y_0 \end{pmatrix}$$

with the stacked output errors on the left hand side and the identity matrix  $I$ . Consequently, solving Equation (8) for  $x_0$  and  $y_0$  requires simple linear algebra only. Only the initial values for the first eight states with the lowest frequencies are estimated to avoid an overfitting of high-order models with more free initial model states. Therefore, the identified model is transformed into a modal representation with sorted eigenvalues before. Furthermore, only the first eight columns and the identity matrix of  $H$  in equation (8) are required.

### 3.3. Model Performance

It is common practice to use the root mean squared (rms) fit error as a performance measure for rotorcraft models. According to ref.<sup>1</sup> the following ratings are used for rms errors

$$(9) \quad \begin{aligned} J_{rms} &\geq 2.0 \text{ to } 3.5 \text{ adequate,} \\ J_{rms} &\geq 1.0 \text{ to } 2.0 \text{ good,} \\ J_{rms} &< 1.0 \text{ excellent to perfect} \end{aligned}$$

for coupled rotorcraft models using scaled velocities in ft/s, angular rates in deg/s and attitudes in

deg. The rms error can be easily interpreted analyzing only one output. Nonetheless, the rms error depends on the physical quantity (or scaling) and the perturbation magnitude of the evaluated time series. Thus, the rms error tend to become inconsistent as a performance measure comprising different outputs like velocities, rates, and the rotor torque from different validation maneuvers.

The Theil inequality coefficient (TIC) normalizes the rms error to the fixed interval between 0 and 1, which is advantageous for model performance comparison. Nonetheless, the TIC is not offset corrected (i.e. shifting both the simulated and measured output by an offset will result in a difference measure). Thus, it is not suitable as a model performance measure.

In the recent publication ref.<sup>16</sup>, different dimensionless criteria have been evaluated to gain a normalized, dimensionless performance measure for time-domain model validation. The index of agreement  $d_1$  was found to give excellent results comparing two time series by a single measure. The index of agreement  $d_1$  is defined as

$$(10) \quad d_1 = \frac{\sum_{i=1}^N |y_{m,k} - y_k|}{\sum_{i=1}^N (|y_{m,k} - \bar{y}_m| + |y_k - \bar{y}_m|)}$$

with the mean of the measured output vector  $\bar{y}_{m,k}$ . The index of agreement  $d_1$  is offset corrected by the measured output mean and ranges from 0 to 1, 1 indicating a perfect match. Since  $d_1$  is a normalized and dimensionless criterion it is not depended on the output scaling nor the perturbation magnitude. The index of agreement is originated in hydrologic and hydroclimatic model validation, see ref.<sup>17</sup>.

To the authors' knowledge, the index of agreement has only been applied to rate a single model output as it is defined to compare two distinct time series. Hence, an overall index of agreement  $\underline{d}_1$  is defined in this paper to rate all outputs of a multiple output model in a one performance measure. As the index of agreement ranges from 0 to 1, the geometric mean is suitable to calculate the overall index of agreement

$$(11) \quad \underline{d}_1 = \prod_{i=1}^{n_y} (d_{1,i})^{\frac{w_i}{n_y}}$$

with the scaling factor for the  $i$ -th output  $w_i$ . In this paper, all scaling factors  $w_i$  are 1. Since the geometric mean is multiplicative, the overall index of agreement  $\underline{d}_1$  is zero, if only one output is zero (i.e. one model output shows low performance).

For the comparison of the rms error  $J_{rms}$  and the index of agreement  $d_1$  an example is given in figure 2 showing the simulated roll rate of two models (1 and 2) and the measured reference (meas)

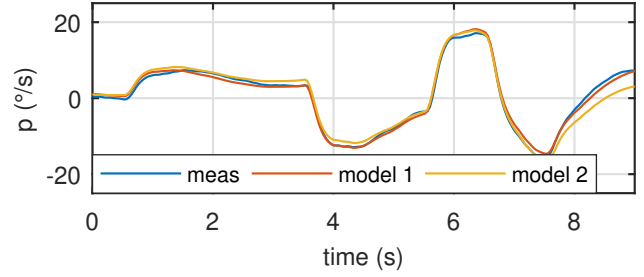


Figure 2: Time series comparison of the roll rate  $p$

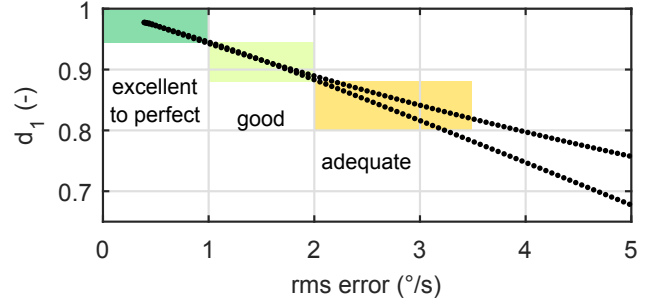


Figure 3: Index of agreement  $d_1$  as a function of the rms error for the maneuver shown in figure 2

of a 3211-multistep maneuver. The performance of model 1 is excellent with  $J_{rms} = 0.82 \text{ }^\circ/s$  and  $d_1 = 0.95$ . Model 2 shows larger differences to the measurement resulting in  $J_{rms} = 1.77 \text{ }^\circ/s$  and  $d_1 = 0.91$ . The index of agreement  $d_1$  is shown as a function of the resulting rms error for the same validation maneuver in figure 3. For one rms error there can be two  $d_1$  depending if the models amplitude is too high or the low.

Based on figure 3 the model performance is rated for an overall index of agreement as

$$(12) \quad \begin{aligned} \underline{d}_1 &\geq 0.80 \text{ to } 0.89 \text{ adequate,} \\ \underline{d}_1 &\geq 0.89 \text{ to } 0.94 \text{ good,} \\ \underline{d}_1 &\geq 0.94 \text{ excellent to perfect.} \end{aligned}$$

All identified models of the ACT/FHS are validated using the overall index of agreement  $\underline{d}_1$ .

## 4. MODEL SELECTION

### 4.1. Model Order

For classical system identification the model order is set beforehand as a model structure is defined based on physical considerations. Often the model order is iteratively increased to cover higher dynamics or submodels of the system to be identified. The PBSIDopt method does not require a predefined model structure, since the states are reconstructed based on the  $n$  largest singular values as described in equation (A.13). Thus, the model order

$n$  is a user-definable variable. In this paper, models with an order between  $n = 8$  and  $n = 20$  are considered. In this way, low-order rotorcraft models as well as high-order models are covered. An appropriate model order is chosen based on the overall index of agreement  $\underline{d}_1$  and physical considerations. For each model order, 4.950 models are identified due to different  $p$  and  $f$  as described before.

In figure 4, the distribution of the overall index of agreement  $\underline{d}_1$  for all identified models is shown with respect to the model order  $n$ . The median of  $\underline{d}_1$  is given by the black solid line, the minimum and maximum values in dotted black. The first and third quartile ( $Q_1$  and  $Q_3$ ) are given in shaded gray. Consequently, 75 % of all models lies between the maximum and  $Q_1$ . As expected, the maximum and median  $\underline{d}_1$  increases with the model order until a certain saturation is reached. The lowest  $\underline{d}_1$  decreases with a growing model order as the model variance increases with increasing model order. The majority of the identified models have adequate fidelity with respect to equation (12) and the best (maximum)  $\underline{d}_1$  are achieved for higher model orders  $n > 15$ .

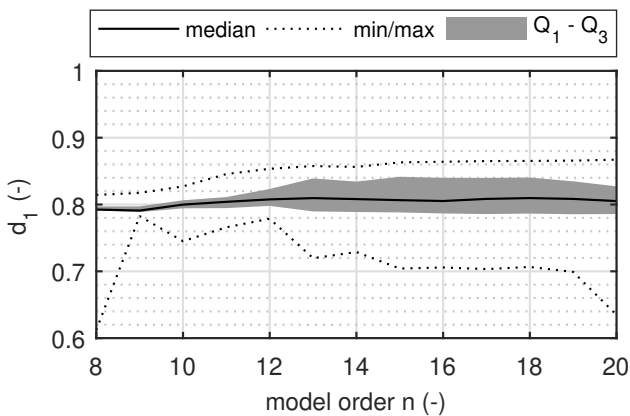


Figure 4: Distribution of overall index of agreement  $\underline{d}_1$  for all models with respect to the model order  $n$

The model order  $n = 12$  is chosen for further evaluation as the overall index of agreement is adequate and it is a common rotorcraft model order. Furthermore,  $n = 18$  is selected to analyze the dynamics of high-order models as well.

#### 4.2. Best Models

In the second step, the best models are selected from all 4.950 identified models as a set for further evaluation. One approach is to select the best 15 % (or any other percentage) of all models. In figure 5a, all transfer functions  $\frac{p}{\delta_y}$  (lateral cyclic input to roll rate) with  $n = 12$  are shown. On the right hand side in figure 5b the best 750 models (15 %) with  $n = 12$  are shown for comparison. All trans-

fer functions are located between the dotted black lines showing the maximum and minimum magnitude. The mean magnitude is shown in solid black, the standard deviation around the mean is depicted in shaded gray. The frequency responses (FR) generated from the flight test sweeps is plotted in blue and transfer function of the best model in red.

The variations between all transfer functions shown in figure 5a is vast for low frequencies  $\omega < 0.4$  rad/s. In addition, several mid-frequency spikes can be found. These effects are originated from weakly damped resonances in some models due to an adverse combination of the PBSIDopt parameters  $p$  and  $f$ . As described before, it is still open research to find the optimal values for  $p$  and  $f$  automatically. Thus, in this paper all possible parameter combination are tested in a parameter study also resulting in models with undesirable properties or/and low performance.

The magnitude variations are reduced considerably regarding only the best 750 models' transfer functions as shown in figure 5b for  $n = 12$ . The standard deviation around the magnitude mean is a narrow band and the mean magnitude in black shows an adequate match with the generated frequency response from the flight test data in blue. Thus, only a few models cause the remaining low frequency variations of the minimum and maximum magnitude. Nonetheless, even the best model (in red) shows an undesired since non-physical low frequency resonance. It is concluded that a selection method based on the model performance index like the overall index of agreement only is not sufficient if the model's purpose is model analysis (e.g. dynamic stability or handling qualities). Therefore, further criteria have to be introduced to select reliable models from all identified ones. Reliable models have to be as good as possible on the one hand, but should not include undesired artifacts like weakly damped resonances without a physical correspondent on the other. In the next subsection, a selection method is introduced to gain such reliable models called "candidate models".

#### 4.3. Candidate Models

In figure 6 the overall index of agreement  $\underline{d}_1$  is shown as a function of the past window length  $p$  to analyze the origin of undesired low frequency resonances described in the last subsection. In blue the  $\underline{d}_1$  of all 4.950 models are shown. The  $\underline{d}_1$  of the selected 750 models from figure 5 are depicted in red. It can be noticed that a high  $\underline{d}_1$  can be found for a past window length between 280 and 500 as well as for  $p \approx p_{max}$ .

A large  $p$  corresponds to a high model order of

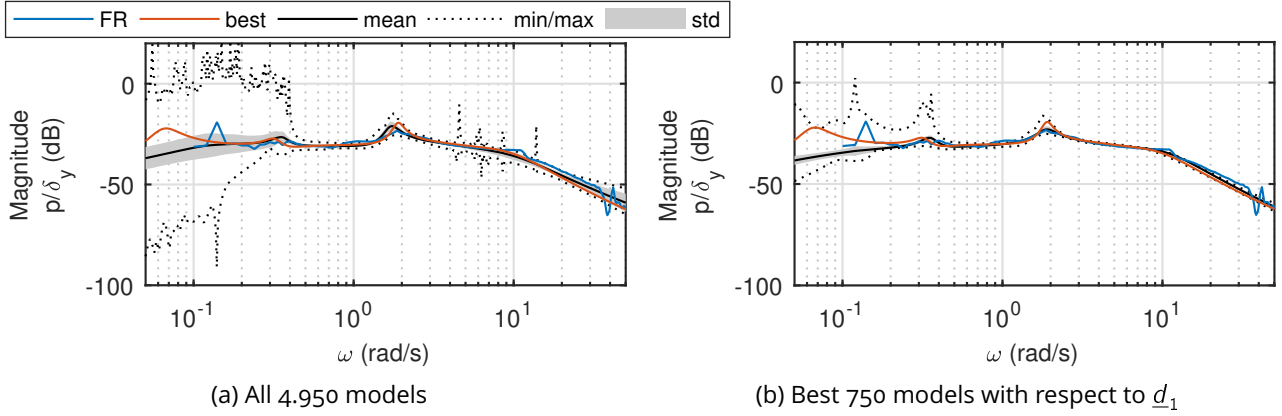


Figure 5: Distribution of identified transfer functions  $p/\delta_y$  for models with  $n = 12$  and measured frequency response

the vector-ARX model estimated in equation (A.9). It is well known that high-order ARX models tend to over-fit data and show high variance even if a regularization method is used,<sup>18,19</sup>. Over-fitting can result in artifacts like weakly damped resonances without physical equivalent. Thus, it is concluded that the high ARX model order (a large  $p$ ) causes these artifacts.

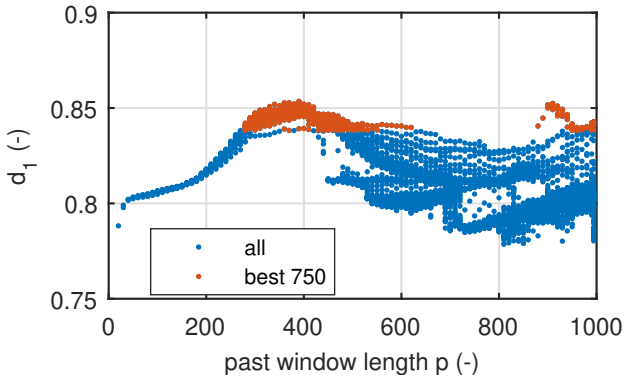


Figure 6: Overall index of agreement  $\underline{d}_1$  as a function of the past window length  $p$  for models with  $n = 12$

An obvious decision would be to exclude large  $p$  from the system identification parameter study. Nevertheless, large past window lengths are beneficial for the estimation of low-order models (i.e.  $n = 8$ ) which are not shown in the paper. In consequence, excluding high  $p$  from system identification would reduce the model performance of low-order models significantly. Several techniques for ARX model order selection can be found in the literature like the (corrected) Akaike Information Criterion, see ref.<sup>18</sup> chapter 16, but these techniques do not provide an useful criterion for model selection in this case.

A suitable criterion is to investigate the predictor form system matrix  $\mathbf{A}_K$ . In equations (A.3) and (A.4) it is assumed that  $\mathbf{A}_K$  is stable to set up the PBSIDopt method. Hence,  $\mathbf{A}_K^p$  have to be (approx-

imately) zero for large  $p$ . This assumption is validated regarding the spectral norm of the predictor form system matrix  $\|\mathbf{A}_K^p\|_2 \approx 0$ .

In figure 7a, the spectral norm of all identified models with  $n = 12$  are shown as a function of the past window length  $p$ . From the selected models of the previous subsection (the best 750 models in red, mostly masked by yellow), the ones with large  $p$  all feature a spectral norm larger than  $10^{-10}$ . Models with small past window lengths also show this behavior.

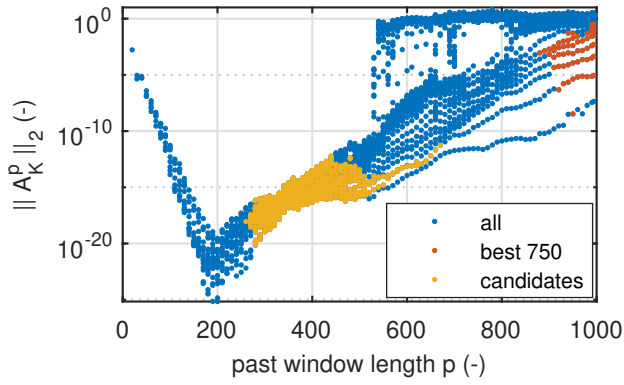
Thus, the method to select candidate models for further evaluation comprises two steps. First, the spectral norm of the identified models is analyzed. Only models with a spectral norm below a defined threshold are accepted:

$$(13) \quad \|\mathbf{A}_K^p\|_2 < 1 \cdot 10^{-10}.$$

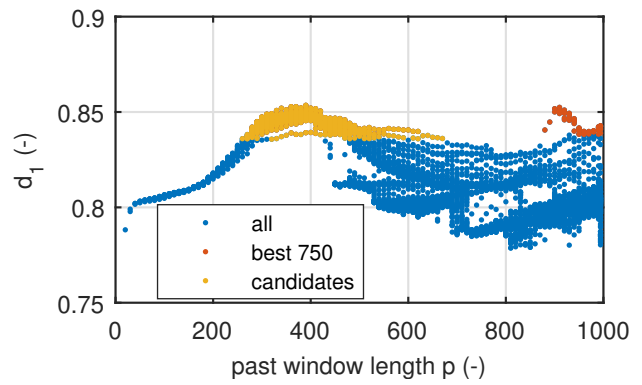
This selection procedure can be applied to low-order as well as to high-order models. In general, low-order models with large  $p$  are accepted since their spectral norm is still nearly zero. High-order models (e.g.  $n = 18$ ) often feature higher spectral norms and the applied limit must be increased  $\|\mathbf{A}_K^p\|_2 < 1 \cdot 10^{-3}$ . Thus, the spectral norm threshold is a used-defined parameter.

In the second step, the best models are selected from the remaining valid ones. The number of selected models should match with the purpose of system identification. In this paper, 750 candidate models are selected with a model order  $n = 12$ , since the probable dynamic stability and HQ are predicted and analyzed. Thus, a high number of models is required to cover a wider range of different models.

The best model shown in figure 5 is not selected as a candidate model, since its spectral norm is too high. The spectral norm and overall index of agreement  $\underline{d}_1$  is shown as a function of the past window length  $p$  for all selected candidate models

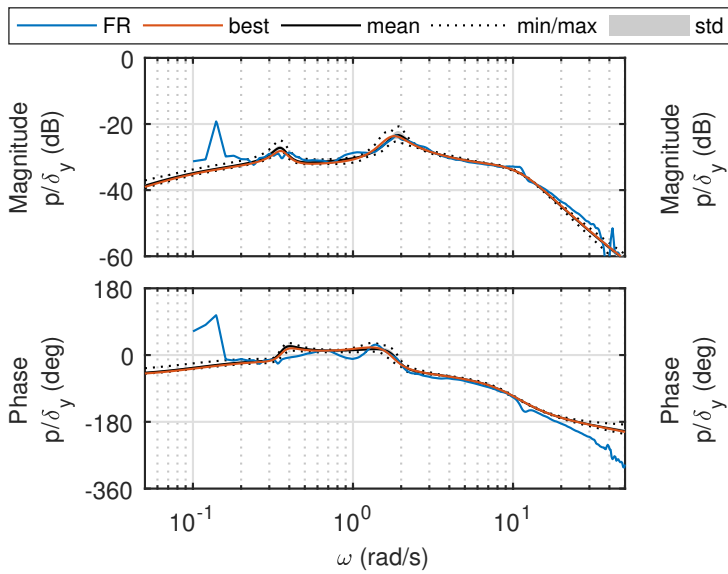


(a) Spectral norm  $\|A_k^p\|_2$  as a function of the past window length  $p$

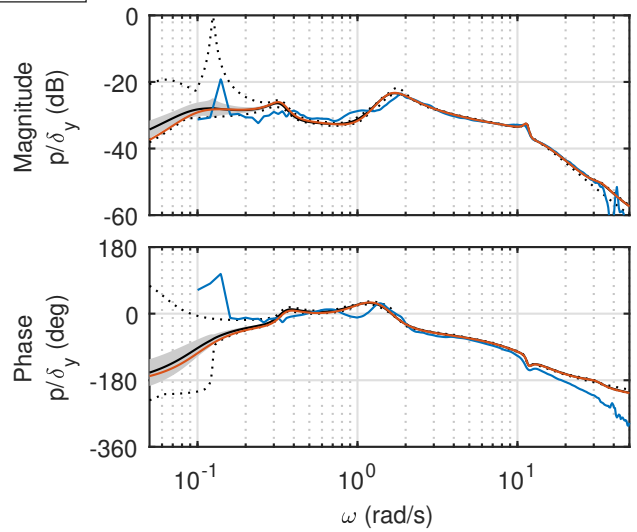


(b) Overall index of agreement  $\underline{d}_1$  as a function of the past window length  $p$

Figure 7: Candidate model criteria for model order  $n = 12$



(a) 750 candidate models,  $n = 12$



(b) 125 candidate models,  $n = 18$

Figure 8: Distribution of identified transfer functions  $p/\delta_y$  for candidate models with  $n = 12$  and  $n = 18$

with  $n = 12$  in figure 7. It can be clearly seen, that models with a high  $p$  are neglected due to their large spectral norm. The selected candidate models with  $n = 12$  have a past window length between 250 and 700, the majority of the candidate models have a  $p$  between 250 and 500.

In figure 8a, the transfer functions  $\frac{p}{\delta_y}$  are shown for the selected candidate models with  $n = 12$ . The magnitude variations are heavily reduced in the low frequency region. Thus, the model invariants only differ slightly from each other. Since the selected candidate models have an adequate overall index of agreement, all candidate models are reliable. Nonetheless, high frequency dynamics like the regressive lead-lag (at about 12 rad/s) are not covered by model with  $n = 12$ , since the model order is too small. For that reason, the candidate models with  $n = 18$  are shown in the same manner in figure 8b.

Here,  $\|A_k^p\|_2 < 1 \cdot 10^{-3}$  is chosen and the number of selected models is reduced to 125. The candidate models are very accurate over the whole frequency range and the regressive lead-lag resonance is covered precisely. The low and mid-frequency dynamics of the candidate models with  $n = 12$  and  $n = 18$  are very similar and the corresponding index of agreement is similar, too. For a larger model order, the variations between the candidate models is increased. This behavior is expected, since the overall model variance is increased for a larger  $n$  as well.

The selected candidate models set up a model set for the analysis of the probable system properties and their uncertainties. The candidate models with  $n = 18$  are further analyzed in the next section, since they provide accurate low to high frequency dynamics.

## 5. MODEL ANALYSIS

Handling qualities (HQ)<sup>20</sup> and dynamic stability<sup>21</sup> are analyzed for 125 selected candidate models with a model order  $n = 18$ . Purpose of this analysis is to evaluate a set of models to have a clear understanding of the possible uncertainty of the HQ and dynamic stability. To select a set of possible models and not only the best model, is well aligned with experience from flight tests with the ACT/FHS: multiple, repeated sweeps and multisteps do usually show a set of possible responses and not the same responses. The candidate models are given as continuous-time state-space models as described in equation (1) with the inputs and outputs according to equation (2). Three kinds of models are in the focus of the model analysis:

- **the bare airframe** as derived by system identification
- **the stabilized vehicle** which is the bare airframe with SCAS (stability control augmentation system) stabilization
- **the optimized vehicle** which is the stabilized vehicle with additional band-stop filter to suppress a 1.8 Hz roll oscillation

Additional input delays, structural notches, and actuator dynamics are not considered for the stabilized and optimized vehicle.

The stabilized vehicle features an output vector feedback that has been extensively used in ACT/FHS flight tests at DLR. Respective feedback equations are:

$$(14a) \quad \text{longitudinal: } \delta_x = \delta_{pilot,x} - K_q q - K_\theta \theta,$$

$$(14b) \quad \text{lateral: } \delta_y = \delta_{pilot,y} - K_p p - K_\phi \phi,$$

$$(14c) \quad \text{pedal: } \delta_p = \delta_{pilot,p} - K_r r.$$

The feedback values were tuned in flight tests and assessed in several campaigns. In detail, the gains are  $K_p = 60$ ,  $K_q = 50$ ,  $K_r = 50$ ,  $K_\phi = 50$ , and  $K_\theta = 60$  where the measurements are given in SI-units and controls in percent (%).

The optimized vehicle is one with improved HQ. It features the SCAS feedback of equation (14) and an additional filter in the roll axis. Ref.<sup>22</sup> showed that roll rate feedback with gains larger approx.  $K_p > 20$  lead to an oscillatory roll motion. The reason for the observed 1.8 Hz oscillation is the so-called regressive lead-lag motion (obtained after transforming the blades' lead-lag motion from the rotating frame to the non-rotating one) which couples with the body-roll fuselage mode. This oscillation is suppressed using the filter proposed in ref.<sup>23</sup>. In detail,

the lateral feedback is modified:

$$(15a) \quad \tilde{\delta}_y = \delta_{pilot,y} - K_p p - K_\phi \phi,$$

$$(15b) \quad \delta_y = \tilde{\delta}_y + K_y \frac{b_2 s^2 + b_1 s}{s^2 + 2D\omega_0 s + \omega_0^2} \tilde{\delta}_y.$$

The coefficients have the values  $K_y = 0.9$ ,  $b_2 = 0.4$ ,  $b_1 = -6$ ,  $D = 0.6$ , and  $\omega_0 = 12.6$ . Compared to ref.<sup>23</sup>, the values were slightly adapted to better fit to the identified models presented in this paper. The longitudinal and pedal axes are not changed by a filter.

### 5.1. Dynamic Stability According to CS27

Dynamic stability as defined by the CS27<sup>21</sup> addresses the system's oscillation characteristics, e.g. values such as time period  $T_P$  and damping coefficient  $D$ . The mean values of these characteristics together with their uncertainty can be calculated using the selected candidate models.

The bare airframe's dynamic stability of the ACT/FHS at 60 knots forward flight is dominated by the phugoid motion, as shown in figure 9 with the grey curves. This pitch rate response was excited using a impulse control input to the bare and stabilized vehicle. The time period and the damping coefficient of the bare vehicle's unstable oscillation are  $T_P = 19.2$  s and  $D = 0.16$ , respectively. The standard deviation of each of these two values is  $\sigma(T_P) = 0.1$  s and  $\sigma(D) = 0.01$ . In case of the stabilized vehicle, the phugoid motion is stable with  $T_P = 4.9$  s and  $D = 0.4$ , see figure 9. In industry application, these values may be used to predict certification specifications from the CS27<sup>21</sup> for instrument flight rules (IFR) in Appendix B on dynamic stability (section VI). Following these requirements, the stabilized vehicle's pitch rate response is predicted to achieve single pilot IFR approval. The bare airframe vehicle is predicted to have dual pilot IFR approval\*.

Although, the SCAS feedback stabilizes the pitch response, a low-damped roll response still remains as shown in figure 10 with the blue curves. This figure shows an impulse input to the lateral control which primarily excites the roll rate. Two fundamental eigenmodes contribute to the stabilized vehicle's weakly damped roll response: the body roll/rotor flap mode ( $T_P = 0.45$  s  $\pm$  0.01 s and  $D = 0.32 \pm 0.02$ ) and the regressive lead-lag mode ( $T_P = 0.55$  s  $\pm$  0.01 s and  $D = 0.03 \pm 0.001$ ). The weakly damped regressive lead-lag oscillation is almost removed from the optimized vehicle response as depicted in figure 10 by the black curves. This is achieved

\*It does not fulfill the single pilot's IFR requirement VI.(a).(3): "Any oscillation having a period of 10 seconds or more but less than 20 seconds must be damped."

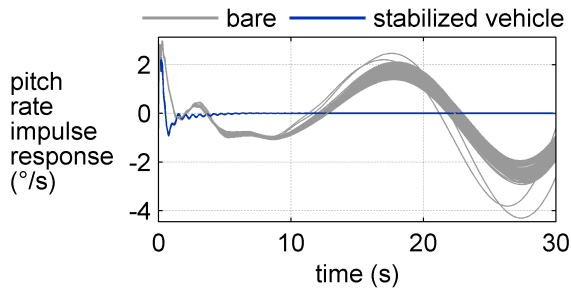


Figure 9: Pitch rate responses due to longitudinal impulse input of the candidate model

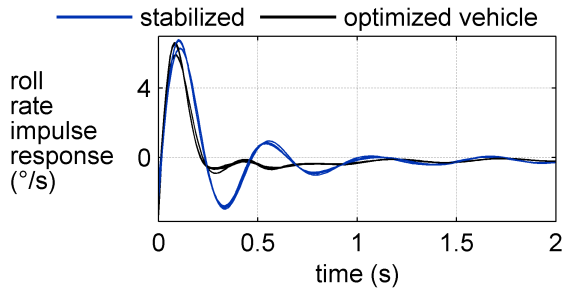


Figure 10: Roll rate responses due to lateral impulse input of the candidate model

ved by the additional filter from equation (15) so that the respective impulse response in figure 10 almost only features the body roll/rotor flap mode ( $T_P = 0.43 \text{ s} \pm 0.01 \text{ s}$  and  $D = 0.58 \pm 0.01$ ). Thus, the optimized vehicle's roll rate response fulfills the CS27<sup>21</sup> IFR single pilot requirements on dynamic stability. As stated in ref.<sup>22</sup>, the suppression of the 1.8 Hz roll oscillation should also improve HQ.

## 5.2. Handling Qualities

HQs are well documented by the Aeronautical Design Standard ADS33<sup>20</sup>. One of the ASD33 criteria is related to dynamic stability. Eigenvalues of the desired response axis are evaluated against the HQ levels. For the MIMO state-space models in equation (1), the desired eigenvalues are extracted based on a reduced SISO transfer function model so that it is assumed that only one axis is piloted and the others remain unchanged. Respective plots of the dynamic stability criteria are provided for the pitch and roll axis in figure 11 and 12.

The pitch axis is dominated by the phugoid motion. Additionally, a low-frequency spiral is added which can hardly be seen in the impulse responses of figure 9 in the time domain. However, the bare airframe has level 2 HQ (gray triangles in figure 11). With SCAS feedback added, the HQ clearly becomes level 1 which correlates well with pilot comments from former ACT/FHS flight tests (blue diamond symbols in figure 11).

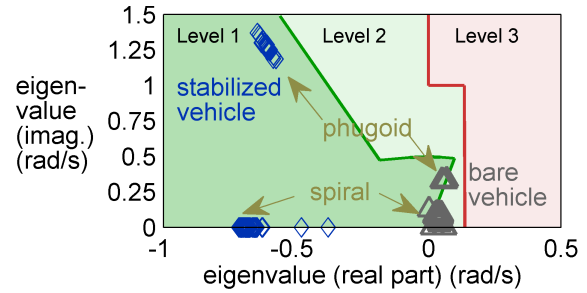


Figure 11: Dynamic stability of the candidate models' pitch axis, ADS33 criteria, compare with figure 9

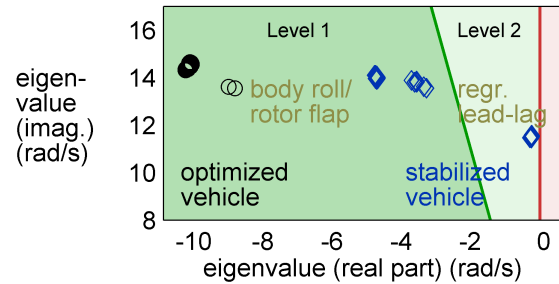


Figure 12: Dynamic stability of the candidate models' roll axis, ADS33 criteria, compare with figure 10

The stabilized vehicle still suffers from a 1.8 Hz roll oscillation which is the regressive lead-lag eigenvalue in figure 12 (blue diamond symbols). Due to this oscillation, the stabilized vehicle only achieves HQ level 2. By adding the filter equation (15), the regressive lead-lag response is suppressed and the body roll/rotor flap eigenvalue (black circles) has a higher frequency. The optimized vehicle is assigned to level 1 HQ.

## 6. CONCLUSIONS

A novel approach for rotorcraft system identification is presented to estimate reliable candidate models from flight test data to predict the possible properties of the system to be identified. The approach comprises a parameter study applying the PBSIDopt method to flight test data of the ACT/FHS research rotorcraft. In this way, thousands linear state-space models of the bare airframe vehicle are identified. A selection method to choose a subset of reliable candidate models from the identified model set is introduced. These chosen candidate models cover the dynamics of the rotorcraft accurately, but have slightly different model invariants. Thus, this subset of candidate models are an excellent choice to predict the possible vehicle characteristics and their uncertainties. In this paper, the candidate models are used to predict dynamic stability as well as HQ of the bare airframe and two diffe-

rent closed-loop configurations. The whole approach can be seen as the second step to provide system identification in rotorcraft series production using the PBSIDopt method as it was suggested in ref.<sup>12</sup>.

The following conclusions are drawn from this work.

1. A normalized and dimensionless model performance index is beneficial for model performance determination and comparison. The index of agreement  $d_1$  is augmented to the overall index of agreement to also rate MIMO models in the time domain.
2. Model order selection based in the overall index of agreement and based on further considerations is suitable as the first step of the model selection procedure.
3. The whole model set with the same model order shows considerable variations regarding the low frequency regions of the corresponding transfer functions. Furthermore, weakly damped resonances can be found which do not have physical equivalents.
4. Selecting only the best 15 % of the identified model set reduces the variance between the selected models. Still, low frequency artifacts occur which are not visible in the time-domain model performance index. Thus, selecting the best model is not sufficient to select reliable candidate models.
5. The spectral norm of the predictor form system matrix is introduced as a further criterion to select candidate models. Models with a spectral norm larger than a certain threshold result in non-physical resonances which are not desired.
6. Hence, the second step of the model selection procedure is the investigation of the before-mentioned spectral norm. Then, the best models of the remaining set are selected as reliable candidate models.
7. The model analysis step rates the dynamic stability and the HQ levels of all candidate models representing the bare airframe of the ACT/FHS. Furthermore, two flight control systems are evaluated. The respective time constants, damping coefficients, and their standard deviations are estimated. The HQ levels correlate well with pilot comments from former ACT/FHS flight tests.

For the future, it is planned to evaluate the herein presented model selection approach combined with the closed-loop system identification maneuvers presented in ref.<sup>12</sup> on the ACT/FHS rotorcraft. In this way, the influence of the system identification parameters  $\hat{f}$  and  $\hat{p}$  will be further analyzed and their suitable ranges may be reduced. In addition, the influence of  $\hat{f}$  and  $\hat{p}$  on the system invariants will be evaluated and a more advanced model selection technique in the frequency domain will be investigated.

Author contact:

Johannes Wartmann, johannes.wartmann@dlr.de  
Dr.-Ing. Steffen Greiser, steffen.greiser@dlr.de

## ACKNOWLEDGMENT

This work was part of the project CHARME within the German Aviation Research Program LuFo V-3 funded by the German Federal Ministry for Economic Affairs and Energy.

Supported by:



Federal Ministry  
for Economic Affairs  
and Energy

on the basis of a decision  
by the German Bundestag

## REFERENCES

- [1] Mark B. Tischler and Robert K. Remple. *Aircraft and Rotorcraft System Identification: Engineering Methods with Flight-Test Examples*. American Institute of Aeronautics and Astronautics, Inc., Reston, Virginia, USA, 2 edition, 2012.
- [2] Susanne Seher-Weiss and Wolfgang von Grünhagen. EC135 System Identification for Model Following Control and Turbulence Modeling. In *Proceedings of the 1st CEAS European Air and Space Conference*, pages 2439–2447, September 2007.
- [3] Steffen Greiser and Susanne Seher-Weiss. A contribution to the development of a full flight envelope quasi-nonlinear helicopter simulation. *CEAS Aeronautical Journal*, 5(1):53–66, March 2014.

- [4] Susanne Seher-Weiss and Wolfgang von Grünhagen. Comparing explicit and implicit modeling of rotor flapping dynamics for the EC 135. *CEAS Aeronautical Journal*, 5(3):319–332, September 2014.
- [5] Susanne Seher-Weiss. Comparing different approaches for modeling the vertical motion of the EC 135. *CEAS Aeronautical Journal*, 6(3):395–406, September 2015.
- [6] Susanne Seher-Weiß. First Attempts to Account for Flexible Modes in ACT/FHS System Identification. In *43rd European Rotorcraft Forum*, Milano, Italy, September 2017.
- [7] Gijs van der Veen, Jan-Willem van Wingerden, Marco Bergamasco, Marco Lovera, and Michel Verhaegen. Closed-loop subspace identification methods: An overview. *IET Control Theory & Applications*, 7(10):1339–1358, July 2013.
- [8] Alessandro Chiuso. The role of vector autoregressive modeling in predictor-based subspace identification. *Automatica*, 43(6):1034–1048, June 2007.
- [9] Alessandro Chiuso. On the Asymptotic Properties of Closed-Loop CCA-Type Subspace Algorithms: Equivalence Results and Role of the Future Horizon. *IEEE Transactions on Automatic Control*, 55(3):634–649, March 2010.
- [10] Johannes Wartmann and Susanne Seher-Weiss. Application of the Predictor-Based Subspace Identification Method to Rotorcraft System Identification. In *39th European Rotorcraft Forum*, Moscow, Russia, September 2013.
- [11] Johannes Wartmann. ACT/FHS System Identification including Engine Torque and Main Rotor Speed using the PBSIDopt Method. In *41st European Rotorcraft Forum*, Munich, Germany, September 2015.
- [12] Johannes Wartmann. Closed-Loop Rotorcraft System Identification Using Generalized Binary Noise. In *American Helicopter Society International 73rd Annual Forum & Technology Display*, Fort Worth, Texas, USA, May 2017.
- [13] Jürgen Kaletka, Hermann Kurscheid, and Ulrich Butter. FHS, the New Research Helicopter: Ready for Service. *Aerospace Science and Technology*, 9(5):456–467, July 2005.
- [14] Johannes Wartmann, Jens Wolfram, and Martin Gestwa. Sensor fusion and flight path reconstruction of the ACT/FHS rotorcraft. *CEAS Aeronautical Journal*, 6(4):529–539, December 2015.
- [15] Simo Särkkä. Unscented Rauch-Tung-Striebel Smoother. *IEEE Transactions on Automatic Control*, 53(3), April 2008.
- [16] Hideo Muroi and Shuichi Adachi. Model Validation Criteria for System Identification in Time Domain. In *17th IFAC Symposium on System Identification SYSID 1015*, Beijing, China, October 2015.
- [17] David R. Legates and Gregpry J. Jr. Mc. Cabe. Evaluating the use of "goodness-of-fit" measures in hydrologic and hydroclimatic model validation. *Water Resources Research*, 35(1):233–241, January 1999.
- [18] Lennart Ljung. *System Identification: Theory for the User*. Prentice Hall PTR, Upper Saddle River, New Jersey, USA, second edition, 1999.
- [19] Lennart Ljung. Some classical and some new ideas for identification of linear systems. *Journal of Control, Automation and Electrical Systems*, 24(1-2):3–10, 2013.
- [20] B. J. Baskett. *ADS-33E-PRF, Aeronautical Design Standard, Performance Specification, Handling Qualities Requirements for Military Rotorcraft*. United States Army Aviation and Missile Command, Aviation Engineering Directorate, Redstone Arsenal, Alabama, 2000.
- [21] EASA. *EASA Certification Specifications for SMALL ROTORCRAFT: CS27 Book 1 Airworthiness code*. European Aviation Safety Agency, 2008.
- [22] Mario Hamers, Robin Lantzsich, and Jens Wolfram. First Control System Evaluation of the Research Helicopter FHS. In *33rd European Rotorcraft Forum*, page 14, Kazan, Russia, September 2007.
- [23] Steffen Greiser and Robin Lantzsich. Equivalent Modelling and Suppression of Air Resonance for the ACT/FHS in Flight. In *39th European Rotorcraft Forum*, Moscow, Russia, 2013.
- [24] Frank Bauer and Mark A. Lukas. Comparing parameter choice methods for regularization of ill-posed problems. *Mathematics and Computers in Simulation*, 81(9):1795–1841, May 2011.
- [25] Lennart Ljung and Tomas McKelvey. Subspace identification from closed loop data. *Signal Processing*, 52(2):209–215, July 1996.

## A. THE PBSIDOPT METHOD

A linear discrete-time state-space model in innovation form with the input vector  $\mathbf{u}_k \in \mathbb{R}^{n_u}$ , the outputs  $\mathbf{y}_k \in \mathbb{R}^{n_y}$  and the states  $\mathbf{x}_k \in \mathbb{R}^n$  is given by

$$(A.1) \quad \begin{aligned} \mathbf{x}_{k+1} &= \mathbf{A}\mathbf{x}_k + \mathbf{B}\mathbf{u}_k + \mathbf{K}\mathbf{e}_k \\ \mathbf{y}_k &= \mathbf{C}\mathbf{x}_k + \mathbf{D}\mathbf{u}_k + \mathbf{e}_k \end{aligned}$$

with the number of inputs  $n_u$ , outputs  $n_y$  and states, i.e. model order  $n$ . The innovations  $\mathbf{e}_k \in \mathbb{R}^{n_y}$  are assumed to be zero-mean white process noise. For the PBSIDopt method a finite set of data points  $\mathbf{u}_k$  and  $\mathbf{y}_k$  with  $k = 1 \dots N$  is considered.

The system in equation (A.1) is transformed into the one-step ahead predictor form assuming that direct feedthrough is absent, i.e.  $D = \mathbf{0}$ ,

$$(A.2) \quad \begin{aligned} \mathbf{x}_{k+1} &= \mathbf{A}_K \mathbf{x}_k + \mathbf{B}_K \mathbf{z}_k \\ \mathbf{y}_k &= \mathbf{C} \mathbf{x}_k + \mathbf{e}_k \end{aligned}$$

with  $\mathbf{A}_K = \mathbf{A} - \mathbf{K}\mathbf{C}$ ,  $\mathbf{B}_K = (\mathbf{B} \ \mathbf{K})$  and  $\mathbf{z}_k = \begin{pmatrix} \mathbf{u}_k \\ \mathbf{y}_k \end{pmatrix}$ . It is furthermore assumed that all eigenvalues of  $\mathbf{A}_K$  are inside the unit circle. Accordingly, the given predictor model in equation (A.2) is stable and the  $(k+p)$ -th state  $\mathbf{x}_{k+p}$  is given by

$$(A.3) \quad \begin{aligned} \mathbf{x}_{k+p} &= \mathbf{A}_K \mathbf{x}_{k+p-1} + \mathbf{B}_K \mathbf{z}_{k+p-1} \\ &= \mathbf{A}_K^p \mathbf{x}_k + \\ &\quad \underbrace{(\mathbf{A}_K^{p-1} \mathbf{B}_K \quad \mathbf{A}_K^{p-2} \mathbf{B}_K \quad \dots \quad \mathbf{B}_K)}_{\mathcal{K}^{(p)}} \begin{pmatrix} \mathbf{z}_k \\ \mathbf{z}_{k+1} \\ \vdots \\ \mathbf{z}_{k+p-1} \end{pmatrix} \end{aligned}$$

and the  $(k+p)$ -th output  $\mathbf{y}_{k+p}$  is

$$(A.4) \quad \mathbf{y}_{k+p} = \mathbf{C} \mathbf{A}_K^p \mathbf{x}_k + \mathbf{C} \mathcal{K}^{(p)} \begin{pmatrix} \mathbf{z}_k \\ \mathbf{z}_{k+1} \\ \vdots \\ \mathbf{z}_{k+p-1} \end{pmatrix} + \mathbf{e}_{k+p}$$

with the extended controllability matrix  $\mathcal{K}^{(p)}$  and the past window length  $p$ . Since  $\mathbf{A}_K$  is stable, the expression  $\mathbf{A}_K^p$  in equations (A.3) and (A.4) can be neglected for large  $p$ :  $\mathbf{A}_K^p \simeq \mathbf{0}$ . Therefore, repeating equations (A.3) and (A.4) for the  $(p+1)$ -th to the  $N$ -th element yields

$$(A.5) \quad \mathbf{X} = \mathcal{K}^{(p)} \mathbf{Z}_p$$

$$(A.6) \quad \mathbf{Y} = \mathbf{C} \mathcal{K}^{(p)} \mathbf{Z}_p + \mathbf{E}$$

with

$$(A.7) \quad \mathbf{X} = \mathbf{X}_{(p+1, N)} = (\mathbf{x}_{p+1} \quad \mathbf{x}_{p+2} \quad \dots \quad \mathbf{x}_N)$$

and the analogous definition for the matrices  $\mathbf{Y}$  and  $\mathbf{E}$ . The merged input-output matrix  $\mathbf{Z}_p$  is defined as

$$(A.8) \quad \mathbf{Z}_p = \mathbf{Z}_{(1, N-p), p} = \begin{pmatrix} \mathbf{z}_1 & \mathbf{z}_2 & \dots & \mathbf{z}_{N-p} \\ \mathbf{z}_2 & \mathbf{z}_3 & \dots & \mathbf{z}_{N-p+1} \\ \vdots & \vdots & \dots & \vdots \\ \mathbf{z}_p & \mathbf{z}_{p+1} & \dots & \mathbf{z}_{N-1} \end{pmatrix}.$$

The predictor Markov parameters  $\mathbf{C} \mathcal{K}^{(p)}$  are estimated in a least-squares sense with Tikhonov regularization to prevent ill-posed problems. The regularized least-squares problem is

$$(A.9) \quad \min_{\mathbf{C} \mathcal{K}^{(p)}} \left( \left\| \mathbf{Y} - \mathbf{C} \mathcal{K}^{(p)} \mathbf{Z}_p \right\|_F^2 + \lambda^2 \left\| \mathbf{C} \mathcal{K}^{(p)} \right\|_F^2 \right).$$

The Strong Robust Generalized Cross Validation method is used to choose the regularization parameter  $\lambda$ , see ref.<sup>24</sup> for more details.

The estimated predictor Markov parameters  $\mathbf{C} \mathcal{K}^{(p)}$  can be interpreted as a high-order vector-ARX model (AutoRegressive model with eXogenous input). High-order ARX models based on equation (A.6) are asymptotically unbiased by correlation issues for large  $N$  and large  $p$ , see ref.<sup>25</sup>. Thus, this step is essential for subspace identification methods like PBSIDopt to provide consistent estimates even in correlated closed-loop experiments.

The extended observability matrix  $\mathcal{O}^{(f)}$  with the future window length  $f$  is introduced

$$(A.10) \quad \mathcal{O}^{(f)} = \begin{pmatrix} \mathbf{C} \\ \mathbf{C} \mathbf{A}_K \\ \vdots \\ \mathbf{C} \mathbf{A}_K^{f-1} \end{pmatrix}.$$

The estimated predictor Markov parameters  $\mathbf{C} \mathcal{K}^{(p)}$  are used to set up the product of extended observability matrix  $\mathcal{O}^{(f)}$  and the extended controllability matrix  $\mathcal{K}^{(p)}$  from equation (A.4)

$$(A.11) \quad \begin{aligned} \mathcal{O}^{(f)} \mathcal{K}^{(p)} &\simeq \\ &\begin{pmatrix} \mathbf{C} \mathbf{A}_K^{p-1} \mathbf{B}_K & \mathbf{C} \mathbf{A}_K^{p-2} \mathbf{B}_K & \dots & \mathbf{C} \mathbf{B}_K \\ \mathbf{0} & \mathbf{C} \mathbf{A}_K^{p-1} \mathbf{B}_K & \dots & \mathbf{C} \mathbf{A}_K \mathbf{B}_K \\ \vdots & \ddots & \ddots & \vdots \\ \mathbf{0} & & & \mathbf{C} \mathbf{A}_K^{f-1} \mathbf{B}_K \end{pmatrix}. \end{aligned}$$

Remembering equation (A.5)

$$(A.12) \quad \begin{aligned} \mathcal{O}^{(f)} \mathbf{X} &= \mathcal{O}^{(f)} \mathcal{K}^{(p)} \mathbf{Z}_p = \mathbf{u} \mathbf{s} \mathbf{v}^T \\ &= (\mathbf{u}_n \quad \mathbf{u}_{\bar{n}}) \begin{pmatrix} \mathbf{S}_n & \mathbf{0} \\ \mathbf{0} & \mathbf{S}_{\bar{n}} \end{pmatrix} \begin{pmatrix} \mathbf{v}_n^T \\ \mathbf{v}_{\bar{n}}^T \end{pmatrix} \end{aligned}$$

the singular value decomposition is applied to reconstruct an estimation of the system states

$$(A.13) \quad \tilde{\mathbf{X}}_{(p+1, N)} = \tilde{\mathbf{X}} = \mathbf{S}_n^{\frac{1}{2}} \mathbf{v}_n^T.$$

The model order  $n$  corresponds to the  $n$  largest singular values in  $\mathbf{S}_n$  used for the state sequence reconstruction.

Finally, the system matrices  $\mathbf{A}$ ,  $\mathbf{B}$ ,  $\mathbf{C}$  and  $\mathbf{K}$  from equation (A.1) are calculated. First,

$$(A.14) \quad \begin{pmatrix} \tilde{\mathbf{X}}_{(p+2, N)} \\ \mathbf{Y}_{(p+1, N-1)} \end{pmatrix} = \begin{pmatrix} \mathbf{A} & \mathbf{B} \\ \mathbf{C} & \mathbf{0} \end{pmatrix} \begin{pmatrix} \tilde{\mathbf{X}}_{(p+1, N-1)} \\ \mathbf{U}_{(p+1, N-1)} \end{pmatrix}$$

is solved for  $\mathbf{A}$ ,  $\mathbf{B}$  and  $\mathbf{C}$  in a least-squares sense. The Kalman gain  $\mathbf{K}$  is then calculated from the covariance matrix of the least-squares residuals and

the system matrices  $\mathbf{A}$  and  $\mathbf{C}$  by solving the stabilizing solution of the corresponding discrete-time algebraic Riccati equation, see ref.<sup>18</sup>.

Since multiple maneuvers are used for system identification of the ACT/FHS, see table 1 in subsection 2.2, all data matrices have to be augmented to consider all maneuvers in one calculation step. For  $j$  maneuvers the output data matrix from equation (A.7) is extended to

$$(A.15) \quad \mathbf{Y} = \left( \mathbf{Y}_{(p+1,N),1} \quad \cdots \quad \mathbf{Y}_{(p+1,N),j} \right).$$

All other data matrices are augmented to use multiple maneuvers in the same way.

Finally, the inverse bilinear transform is then applied to calculate the continuous-time state-space model

$$(A.16) \quad \begin{aligned} \dot{\mathbf{x}} &= \mathbf{A}_{ct} \mathbf{x} + \mathbf{B}_{ct} \mathbf{u} \\ \mathbf{y} &= \mathbf{C}_{ct} \mathbf{x}. \end{aligned}$$

The estimated system matrices in equation (A.14) and equation (A.16) are fully populated and do not represent physical quantities. The identified model can be transformed so that the first  $n_y$  states correspond to the outputs  $y$  using the transformation described in ref.<sup>11</sup>.